PHYSICAL REVIEW A **85**, 052704 (2012)

Single and multiple electron removal processes in proton–water-molecule collisions

Mitsuko Murakami, Tom Kirchner,[*] and Marko Horbatsch
Department of Physics and Astronomy, York University, Toronto, Ontario, Canada M3J 1P3

Hans Jürgen Lüdde
Institut für Theoretische Physik, Goethe-Universität, D-60438 Frankfurt, Germany

(Received 31 March 2012; published 10 May 2012)

Charge-state correlated cross sections for single- and multiple-electron removal processes (capture and ionization) in proton-H_2O collisions are calculated by using the nonperturbative basis generator method adapted for ion-molecule collisions [Phys. Rev. A **80**, 060702(R) (2009)]. The results are compared with experimental data for a wide range of impact energies spanning from 20 keV to several MeV. Single-electron removal probabilities in each molecular orbital are evaluated using the inclusive-probability formalism to predict the yields of charged fragments (H_2O^+, OH^+, H^+, O^+) according to branching ratios that are valid at high impact energies. At intermediate and low energies, we calculate improved fragmentation cross sections that include the effects of multiple-electron removal processes. The resulting fragmentation yields agree with experiments at the 20%–30% level even below 100 keV impact energy.

DOI: 10.1103/PhysRevA.85.052704 PACS number(s): 34.10.+x, 34.50.Gb, 34.70.+e

I. INTRODUCTION

Collisions of water molecules with ions represent an important problem for both practical and fundamental reasons. Understanding the collision-induced fragmentation of water molecules is essential in some areas of applied science, such as atmospheric research, radiation and ion-beam tumor treatment, collider technology, and nuclear safety (see [1,2] and references therein). From a basic physics point of view, ion–water-vapor collisions offer a wealth of interesting questions concerning many-body theory. In comparison to atomic targets, the water molecule poses substantial challenges associated with its multicenter geometry [3–7] and additional degrees of freedom such as fragmentation and nuclear motion (rotation and vibration).

Calculations of ion–water-vapor collisions at projectile energies above 20 keV, for which electronic correlation during the collision is deemed unimportant, can be based on relatively simple self-consistent field wave functions. Such works include a recent molecular-orbital (MO) based method for energies below about 100 keV [7], Born-type calculations valid in the high-energy limit [6,8], and the continuum distorted-wave approach [9]. A recent work by Illescas *et al.* [5] applies the three-center classical trajectory Monte Carlo (CTMC) method to study collisions of protons, He^{2+}, and C^{6+} with water vapor. Their work addresses an important question of double-electron removal processes at low impact energies where transfer ionization (i.e., one electron is captured, and another is ionized) may affect fragmentation cross sections in a manner unpredicted by the first-order Born approximation (see also Refs. [1,10]).

Recently, we reported on a nonperturbative, quantum-mechanical approach to ion-molecule collisions in an independent-particle model (IPM) framework using the basis generator method (BGM) [11]. A mathematical foundation of the BGM can be found in Ref. [12]. On the practical side, BGM calculations have been tested for many instances of ion-atom collisions with both bare and dressed projectiles (see, e.g., Refs. [13–15] and the review article [16]). The adaptation of the BGM to ion-H_2O collisions was accomplished by (i) a spectral representation of the molecular Hamiltonian, and (ii) a basis expansion of the molecular wave function in terms of density-functional-theory–based (DFT-based) atomic orbitals (AOs). For proton [11] and He^+ [17] impact, it was demonstrated that net cross sections of various electron transfer processes (capture, ionization, and projectile loss) are well described by this approach for a wide range of impact energies between 20 and 5000 keV/amu.

In this work, we present a more comprehensive description of the ion-molecule BGM approach [11] and extend the previous study of proton-H_2O collisions to calculate the cross sections of single- and multiple-electron removal processes leading to fragmentation. The paper is organized as follows: The BGM formalism for proton-H_2O collisions is described in Sec. II A, with some technical details being relegated to the Appendix. In Sec. II B, methods of analysis to calculate the charge-state correlated cross sections and the fragmentation yields are explained. The results are presented in Sec. III, followed by conclusions in Sec. IV. Atomic units ($\hbar = m_e = e = 4\pi\epsilon_0 = 1$) are used throughout, unless specified otherwise.

II. THEORY

The collisions considered in this work (for impact energies of 20 keV up to several MeV) are sufficiently fast to ensure that the target molecule neither rotates nor vibrates appreciably while it interacts with the projectile. Furthermore, the semiclassical approximation can be used in its simplest form, in which the projectile passes by the (fixed-in-space) molecule on a straight-line trajectory. We are thus left with the task of solving the time-dependent Schrödinger equation (TDSE) for the many-electron system in an IPM framework, followed by the task to extract measurable information, such as charge-state correlated and fragmentation cross sections from its solution. We first describe theoretical and practical aspects

---

[*] tomk@yorku.ca

of our approach to the (approximate) solution of the TDSE in Sec. II A and then discuss methods to extract the cross sections of interest in Sec. II B.

A. Collision dynamics

1. Formulation

The full many-electron TDSE under discussion cannot be solved directly due to the multicenter geometry and the presence of the electron-electron interaction. Hence, we address a simplified problem in which the electronic Hamiltonian is assumed to be of single-particle form such that the TDSE separates into a set of single-particle equations for the initially occupied MOs:

$$i\partial_t \left|\psi^{\Gamma}_{\alpha\beta\gamma}(t)\right\rangle = \left[\hat{H}^T_{\alpha\beta\gamma} + V^P(t)\right]\left|\psi^{\Gamma}_{\alpha\beta\gamma}(t)\right\rangle, \tag{1}$$

$$\left|\psi^{\Gamma}_{\alpha\beta\gamma}(t_i)\right\rangle = |\Gamma_{\alpha\beta\gamma}\rangle, \tag{2}$$

$$\hat{H}^T_{\alpha\beta\gamma} = -\frac{1}{2}\nabla^2 + V^T_{\alpha\beta\gamma}, \tag{3}$$

$$V^P(t) = -\frac{Q_P}{|\vec{r}-\vec{R}(t)|}. \tag{4}$$

We use capital Greek letters to label the MOs; namely, $\Gamma_{\alpha\beta\gamma} \in \{1b_1, 3a_1, 1b_2, 2a_1\}_{\alpha\beta\gamma}$ denotes the four outer MOs of H_2O for a given molecular orientation specified by the Euler angles α, β, γ [11]. We exclude the innermost orbital $1a_1$, since test calculations show that electrons in this MO do not undergo appreciable transitions in the collisions investigated in this work. $V^T_{\alpha\beta\gamma}$ is an effective target potential, Q_P is the charge of the projectile ($Q_P = 1$ for protons), and $\vec{R}(t) = (b,0,v_o t)$ defines the straight-line trajectory. The impact parameter b is the perpendicular distance between the projectile and the oxygen nucleus, and v_o is the (constant) projectile speed. For the general formulation of the theory we choose the oxygen nucleus as the origin of the coordinate system (see Fig. 1), while the numerical calculations are performed in a center-of-mass (c.m.) frame (see Appendix).

We now outline the general ideas of our approach to solving the single-particle equations (1). More practical and technical aspects of the actual implementation within the two-center (TC) version of the BGM are discussed in the next subsection and in the Appendix.

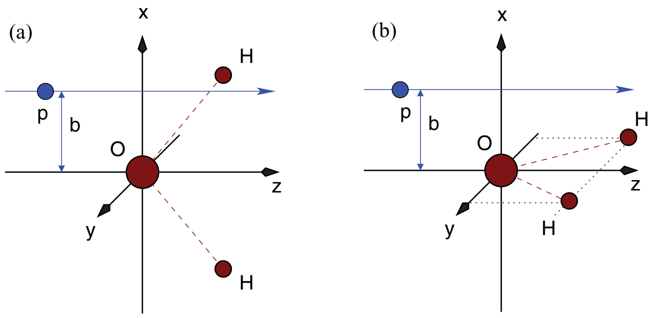

FIG. 1. (Color online) Geometries of the proton-H_2O collision system. (a): (0, 0, 0) configuration; (b): (90, 0, 0) configuration.

Let us assume that the solutions of Eq. (1) are expanded in a time-dependent, nonorthogonal basis

$$\left|\psi^{\Gamma}_{\alpha\beta\gamma}(t)\right\rangle = \sum_j a^{\Gamma}_{j,\alpha\beta\gamma}(t)|\chi_j(t)\rangle. \tag{5}$$

This turns the single-particle equations into a set of coupled-channel equations for the expansion coefficients:

$$\begin{aligned} i\sum_{j=1} \dot{a}^{\Gamma}_{j,\alpha\beta\gamma}(t)\langle\chi_k(t)|\chi_j(t)\rangle \\ = \sum_{j=1} a^{\Gamma}_{j,\alpha\beta\gamma}(t)\langle\chi_k(t)|\hat{H}^T_{\alpha\beta\gamma} + V^P(t) - i\partial_t|\chi_j(t)\rangle. \end{aligned} \tag{6}$$

The goal of the present approach is to avoid the explicit calculation of multicenter integrals. To this end, we introduce the spectral representation of the molecular target Hamiltonian

$$\hat{H}^T_{\alpha\beta\gamma} = \sum_{\Lambda} \epsilon_{\Lambda}|\Lambda_{\alpha\beta\gamma}\rangle\langle\Lambda_{\alpha\beta\gamma}|, \tag{7}$$

in which ϵ_{Λ} denotes the energy eigenvalue of the MO labeled by quantum number(s) Λ. If we represent the MOs in an orthonormal single-center basis $\{|s\rangle\}$ (where s in practice is a multi-index),

$$|\Lambda_{\alpha\beta\gamma}\rangle = \sum_s d^{\Lambda}_{s,\alpha\beta\gamma}|s\rangle, \tag{8}$$

the multicenter molecular matrix element in Eq. (6) breaks up into a combination of energy eigenvalues, (real) expansion coefficients, and simpler overlap matrix elements:

$$\begin{aligned} M_{kj}(t) &\equiv \langle\chi_k(t)|\hat{H}^T_{\alpha\beta\gamma}|\chi_j(t)\rangle \\ &= \sum_{\Lambda}\sum_{su} \epsilon_{\Lambda}\langle\chi_k(t)|s\rangle d^{\Lambda}_{s,\alpha\beta\gamma} d^{\Lambda}_{u,\alpha\beta\gamma}\langle u|\chi_j(t)\rangle. \end{aligned} \tag{9}$$

Our strategy of bypassing the multicenter terms is completed by making use of the linearity of the single-particle equations (1) and propagating the single-center basis states $|s\rangle$ rather than the multicenter MOs. Accordingly, the states

$$\left|\psi^{s}_{\alpha\beta\gamma}(t)\right\rangle = \sum_j a^{s}_{j,\alpha\beta\gamma}(t)|\chi_j(t)\rangle \tag{10}$$

obtained from solving the coupled-channel equations (6) while using the states $|s\rangle$ as initial conditions are combined to reconstruct the solutions $|\psi^{\Gamma}_{\alpha\beta\gamma}\rangle$ of Eq. (1):

$$\left|\psi^{\Gamma}_{\alpha\beta\gamma}(t)\right\rangle = \sum_s d^{\Gamma}_{s,\alpha\beta\gamma}\left|\psi^{s}_{\alpha\beta\gamma}(t)\right\rangle = \sum_{sj} d^{\Gamma}_{s,\alpha\beta\gamma} a^{s}_{j,\alpha\beta\gamma}(t)|\chi_j(t)\rangle. \tag{11}$$

Essentially, the outlined approach results in a separation of the collision dynamics and the molecular geometry problem: except for the matrix element (9) the coupled-channel equations to be solved are similar to those of an ion-atom collision problem. The molecular orientation is accounted for at the end by combining those solutions using the coefficients $d^{\Gamma}_{s,\alpha\beta\gamma}$ according to Eq. (11). Note that, in principle, the approach does not involve any approximation. It does, however, in practice since all the expansions need to be finite.

2. Practical aspects

Three expansions appear in the approach described in the previous section: (i) for the spectral representation of the molecular Hamiltonian $\hat{H}^T_{\alpha\beta\gamma}$, (ii) for the representation of the MOs $|\Gamma_{\alpha\beta\gamma}\rangle$, and (iii) for the propagation of the orbitals $|\psi^s_{\alpha\beta\gamma}(t)\rangle$.

For the single-centered representation of the (occupied) MOs we use a set of oxygen AOs obtained from a DFT calculation based on the exchange-only limit of the optimized potential method [18]. All orbitals of the KLM shells are included to re-expand the minimal-basis-set MOs $|\tilde{\Gamma}_{\alpha\beta\gamma}\rangle$ of Ref. [19]. This yields the total norm integrals

$$0.9 \leqslant \sum_{s}^{KLM} |\langle s|\tilde{\Gamma}_{\alpha\beta\gamma}\rangle|^2 < 1, \tag{12}$$

which is deemed acceptable, but not perfect. Note that we readjust the normalization of the approximated MOs to allow for a standard statistical interpretation of the propagated states; namely, the expansion coefficients in Eq. (8) are calculated as

$$d^{\Gamma}_{s,\alpha\beta\gamma} = \frac{\langle s|\tilde{\Gamma}_{\alpha\beta\gamma}\rangle}{\sum_{s'}^{KLM} |\langle s'|\tilde{\Gamma}_{\alpha\beta\gamma}\rangle|^2}. \tag{13}$$

The spectral representation of the molecular Hamiltonian (7) is limited to the initially occupied MOs $\{1b_1, 3a_1, 1b_2, 2a_1\}$ given in the single-center basis detailed above. This means that contributions from excited and continuum states are neglected. We have carried out some tests by including these contributions approximately in terms of a closure approximation

$$\begin{aligned}\hat{H}^T_{\alpha\beta\gamma} &= \sum_{\Lambda}^{\text{occ}} \epsilon_\Lambda |\Lambda_{\alpha\beta\gamma}\rangle\langle\Lambda_{\alpha\beta\gamma}| + \sum_{\Lambda}^{\text{unocc}} \epsilon_\Lambda |\Lambda_{\alpha\beta\gamma}\rangle\langle\Lambda_{\alpha\beta\gamma}| \\ &\approx \sum_{\Lambda}^{\text{occ}} \epsilon_\Lambda |\Lambda_{\alpha\beta\gamma}\rangle\langle\Lambda_{\alpha\beta\gamma}| + \bar{\epsilon} \sum_{\Lambda}^{\text{unocc}} |\Lambda_{\alpha\beta\gamma}\rangle\langle\Lambda_{\alpha\beta\gamma}| \\ &= \sum_{\Lambda}^{\text{occ}} (\epsilon_\Lambda - \bar{\epsilon}) |\Lambda_{\alpha\beta\gamma}\rangle\langle\Lambda_{\alpha\beta\gamma}| + \bar{\epsilon}\end{aligned} \tag{14}$$

and found no significant changes in the net cross sections [11].

For the propagation, we use the same TC-BGM basis as in our previous work [11]. It consists of AOs placed on the target center (the oxygen nucleus) and the projectile, as well as a set of 22 BGM (pseudo) states which represent the continuum at large separations between projectile and target. The set of target AOs is identical with the set of orbitals used for the single-centered representation of the MOs (8), while on the projectile we include all hydrogen orbitals of the $KLMN$ shells. We have checked that this TC-BGM basis produces well-converged results for the proton-oxygen ion-atom collision system, which was investigated some time ago with a differently constructed BGM basis [13].

Since the coupled-channel equations at hand are similar to those of an ion-atom collision problem only a few changes in the implementation of the TC-BGM were necessary to carry out the propagation. Some details on the basis and the calculation of the required matrix elements are given in the Appendix.

B. Final-state analysis and extraction of measurable cross sections

1. Single- and multiple-electron transition probabilities

Our analysis of capture and ionization processes is based on the inclusive-probability formalism of Ref. [20]. This analysis assumes that the propagated N-electron state and all final states of interest are represented as single Slater determinants (i.e., the Pauli principle is taken into account). One can show that the transition probabilities for single- and multiple-electron processes can then be calculated from determinants of the one-particle density matrix,

$$\begin{aligned}\langle f|\hat{\gamma}^1(t_f)|f'\rangle &= \sum_{i=1}^{N} \langle f|\psi_i(t_f)\rangle\langle\psi_i(t_f)|f'\rangle \\ &= \sum_{i=1}^{N} A_{if}(t_f)A^*_{if'}(t_f),\end{aligned} \tag{15}$$

at a sufficiently large final time t_f. In practice, we choose t_f such that the projectile's distance from the oxygen nucleus equals 40 a.u. for all impact parameters and energies. The propagated states in Eq. (15) are those of Eq. (11), and as final states $|f\rangle$ we consider bound projectile states $|k_P\rangle$ and bound target states $|\Gamma_{\alpha\beta\gamma}\rangle$. The former are part of the (orthogonalized) TC-BGM basis such that we obtain

$$A^P_{if}(t_f) = \langle k_P\,|\psi^\Gamma_{\alpha\beta\gamma}(t_f)\rangle = \sum_{s}^{T} d^\Gamma_{s,\alpha\beta\gamma} a^s_{k,\alpha\beta\gamma}(t_f), \tag{16}$$

with the sum running over all included (atomic) target states. For the target amplitudes we use the expansion (8) and obtain

$$A^T_{if}(t_f) = \langle\Lambda_{\alpha\beta\gamma}\,|\psi^\Gamma_{\alpha\beta\gamma}(t_f)\rangle = \sum_{s,t}^{T} d^\Lambda_{t,\alpha\beta\gamma} d^\Gamma_{s,\alpha\beta\gamma} a^s_{t,\alpha\beta\gamma}(t_f). \tag{17}$$

Note that all amplitudes and hence all density matrix elements and probabilities to be extracted from them depend on the Euler angles (i.e., the orientation of the molecule).

We are interested in two types of probabilities: (i) the probabilities $P_{k,l}$ of k-fold capture in coincidence with l-fold ionization to the continuum, and (ii) the probability for the production of exactly one vacancy in one of the ground-state MOs. The latter corresponds to a particle-hole probability and is calculated according to [20]

$$P^{\bar{f}_1}_{f_1\ldots f_{N-1}} = P_{f_1\ldots f_{N-1}} - P_{f_1\ldots f_{N-1},\bar{f}_1}, \tag{18}$$

where $P_{f_1\ldots f_{N-1}}$ denotes the *inclusive* probability for finding $N-1$ electrons in the subconfiguration $|f_1\ldots f_{N-1}\rangle$, and $P_{f_1\ldots f_{N-1},\bar{f}_1}$ is the *exclusive* probability to find N electrons in the configuration $|f_1\ldots f_{N-1}\bar{f}_1\rangle$. Obviously, the difference of both probabilities corresponds to the statement that one of the electrons can be found anywhere except in the state $|\bar{f}_1\rangle$, which is vacant.

The calculation of the $P_{k,l}$ is more involved. One first needs to define subspaces of the one-particle Hilbert space that correspond to finding a single electron bound to the projectile or to the target, respectively. For the projectile subspace we consider all hydrogen orbitals of the $KLMN$ shells (i.e., the same set of states that is used in the TC-BGM calculation). The target subspace is restricted to the initially populated MOs. This is consistent with the neglect of excited states in the spectral representation of the target Hamiltonian, but is an additional approximation that excludes target excitation. The unitarity of the problem implies that electrons which are neither found in one of the projectile AOs, nor in one of the target MOs are being transferred to the continuum. One can show that the $P_{k,l}$ can then be calculated from ordered sums of inclusive probabilities for occupying bound target and bound projectile states only [see Eqs. (18) to (20) of Ref. [14]].

The probabilities for net q-fold capture and ionization are found from the $P_{k,l}$ as

$$P_q^{\text{cap}} = \sum_{l=0}^{N-q} P_{q,l}, \quad P_q^{\text{ion}} = \sum_{k=0}^{N-q} P_{k,q}. \tag{19}$$

They are related to total net (sometimes also called gross) electron numbers by

$$P_{\text{cap}} = \sum_{q=1}^{N} q P_q^{\text{cap}}, \quad P_{\text{ion}} = \sum_{q=1}^{N} q P_q^{\text{ion}}. \tag{20}$$

Note that the net electron numbers can also be obtained from summing up single-particle probabilities according to [21]

$$P_{\text{cap}} = \sum_{i=1}^{N} \sum_{f}^{P} \left|A_{if}^{P}\right|^2, \quad P_{\text{ion}} = N - P_{\text{cap}} - \sum_{i=1}^{N} \sum_{f}^{T} \left|A_{if}^{T}\right|^2, \tag{21}$$

which serves as a consistency test.

Even though multiple-electron removal ($q > 1$) is less likely than single-electron capture or single ionization, sizable contributions to the net electron numbers arise because of the factor of q in Eq. (20). For capture this can pose the following challenge: if we propagate N target electrons, the calculated average number of captured electrons P_{cap} can exceed the number of electrons that can be bound to the projectile proton. We will show in Sec. III A how to deal with this problem in a pragmatic way.

2. *Orientation-averaged cross sections*

As mentioned above, the calculated capture and ionization probabilities depend on the orientation of the molecule with respect to the ion beam direction. This information is not available in the experimental data we wish to compare with; hence, we have to average our results in an appropriate way. As discussed in Ref. [11], we found a noticeable orientation dependence at the lower end of the considered impact-energy interval, but very similar results for net capture and net ionization when we calculated partial averages (i) for the water molecule being rotated within the scattering plane, and (ii) for the water molecule being rotated about the projectile beam axis. This is exploited in the present work in the same way as in Ref. [11]: We approximate the fully angle-averaged cross section for a given process by

$$\sigma = \int P(b;\, \alpha,\beta = 0,\gamma = 0) d^2 b. \tag{22}$$

The basic orientation $(\alpha,\beta,\gamma) = (0,0,0)$ is chosen such that the polar angle of the impact parameter vector $\mathbf{b}$ coincides with α if $\beta = \gamma = 0$ [see Fig. 1(a)]. Symmetry requires the transition probability P to be π periodic in α and to assume extremum values at $\alpha = 0$ and $\alpha = \pi/2$. These properties are captured by the sinusoidal ansatz

$$P(b;\alpha,\beta = 0,\gamma = 0) = A(b)[\cos(2\alpha) + B(b)], \tag{23}$$

$$A = \frac{1}{2}[P(b;\, 0,0,0) - P(b;\, \pi/2,0,0)], \tag{24}$$

$$B = \frac{1}{2A}[P(b;\, 0,0,0) + P(b;\, \pi/2,0,0)]. \tag{25}$$

Inserting this into Eq. (22) results in

$$\sigma = \pi \int_0^\infty b\left[P(b;\, 0,0,0) + P\left(b;\, \frac{\pi}{2},0,0\right)\right] db \tag{26}$$

after carrying out the angular integral. Accordingly, we calculate the angle-average of the two orientations $(\alpha,\beta,\gamma) = (0,0,0)$ and $(\alpha,\beta,\gamma) = (\pi/2,0,0)$ (see Fig. 1) to replicate the effect of randomly oriented water molecules [i.e., all cross sections reported in Sec. III are obtained from using Eq. (26)]. While this limited angle-averaging is found to be sufficient for the purpose of obtaining net and charge-state correlated cross sections for electron removal, it becomes a problem when evaluating the single-vacancy cross sections for each MO which form the basis of the fragmentation analysis outlined in the next subsection.

3. *Fragmentation cross sections*

Collision-induced electron removal from a water molecule produces four different singly charged (fragment) ions (H_2O^+, OH^+, H^+, and O^+) in measurable amounts in addition to traces of $H_2{}^+$ and O^{2+} [22]. In the high-impact-energy limit, the fragmentation cross sections of these four ions can be estimated on the basis of the empirical branching ratios of Tan *et al.* [23] as

$$\sigma_{H_2O^+} = 1.00\sigma_{1b_1}^S + 1.00\sigma_{3a_1}^S + 0.08\sigma_{1b_2}^S, \tag{27}$$

$$\sigma_{OH^+} = 0.70\sigma_{1b_2}^S, \tag{28}$$

$$\sigma_{H^+} = 0.22\sigma_{1b_2}^S + 0.74\sigma_{2a_1}^S, \tag{29}$$

$$\sigma_{O^+} = 0.26\sigma_{2a_1}^S, \tag{30}$$

where $\sigma_{\Gamma\in\{1b_1,3a_1,1b_2,2a_1\}}^S$ are the cross sections for single-electron removal (due to capture or ionization) from each MO. They are calculated based on the inclusive-probability analysis using Eq. (18).

III. RESULTS

A. Charge-state correlated cross sections

Figure 2 shows a comparison of cross sections for capture processes. At the top we compare the BGM-based net capture cross section (solid line) with the experimental data of Rudd *et al.* [24] and Toburen *et al.* [25]. There is good overall agreement with these data except at the higher impact energies (above 200 keV). One can argue that the present calculation for net capture agrees at the 20%–30% level (or better) for low to

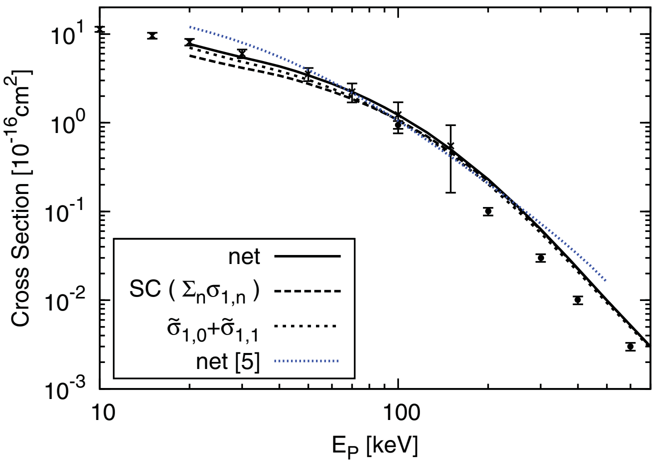

FIG. 2. (Color online) Cross sections for net electron capture (net) and for single-electron capture (SC) in proton-H_2O collisions. The theoretical results are obtained from the inclusive-probability analysis and an average over the (0, 0, 0) and ($\pi/2$, 0, 0) molecular orientations. Also shown is the modified SC ($\tilde{\sigma}_{1,0} + \tilde{\sigma}_{1,1}$) [cf. Eqs. (31) and (32)]. Experimental data are for net electron capture: (×) [24], (●) [25]. Also shown with the dotted (blue) line is the theoretical cross section from Ref. [5] for net electron capture.

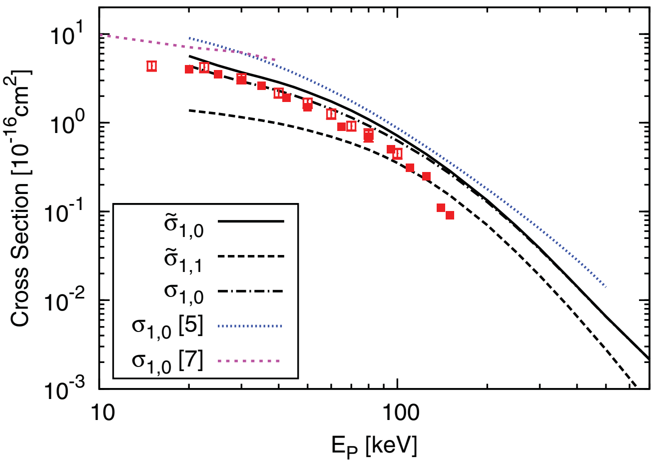

FIG. 3. (Color online) Cross sections for pure single-electron capture ($\tilde{\sigma}_{1,0}$) given by Eq. (31), and for transfer ionization ($\tilde{\sigma}_{1,1}$) given by Eq. (32), based on the inclusive-probability analysis and an average over the (0, 0, 0) and ($\pi/2$, 0, 0) molecular orientations. Also shown with the dash-dotted line is the pure single-electron capture $\sigma_{1,0}$ without the correction to redefine double-electron capture as single-electron capture [cf. Eq. (31)]. Experimental data are for H_2O^+ ion production in the capture channel of Refs. [22] (■) and [27] (□), which serves as a lower bound for $\tilde{\sigma}_{1,0}$. The theoretical cross sections from Ref. [5] and those from method I of Ref. [7] for pure single-electron capture are shown with a blue and a magenta dotted line, respectively.

intermediate energies. The CTMC calculation of Ref. [5] (blue dotted line) agrees with experiments at intermediate energies, but overestimates them both at low and at high impact energies.

Also shown as a dashed line in Fig. 2 is the single-electron capture (SC) cross section obtained from Eq. (19) for $q = 1$. The difference between the theoretical net capture and SC cross sections at low to intermediate energies shows that the inclusive-probability analysis is problematic for the case of a proton projectile: the IPM-BGM predicts predominantly capture into the H(1*s*) state. The Pauli principle allows two electrons with antiparallel spins to be captured, whereas in reality formation of the negative hydrogen ion is a correlated process with small probability. In the context of proton-atom collisions, a statistical treatment using a product-of-binomials analysis was proposed to deal with the double-electron capture problem [13]; the entire net capture cross section was associated with SC. The presently employed inclusive-probability analysis does suppress unphysical higher-order ($q > 2$) capture cross sections. A pragmatic way to correct the problem, therefore, is to sum over the double-electron capture channels weighted by a multiplicity and to associate the result with SC. That is, we define the pure SC and transfer ionization in our calculation as

$$\tilde{\sigma}_{1,0} = \sigma_{1,0} + 2\sigma_{2,0}, \qquad (31)$$

$$\tilde{\sigma}_{1,1} = \sigma_{1,1} + 2\sigma_{2,1}, \qquad (32)$$

where $\sigma_{k,l}$ are the cross sections for k-fold capture in coincidence with l-fold ionization corresponding to the probabilities $P_{k,l}$ discussed in Sec. II B1. Carrying out such a reinterpretation results in the dotted line in Fig. 2, and it accounts for most of the net capture cross section. The difference indicates that electron transfer accompanied by multiple ionization is not negligible at intermediate energies according to the present IPM-BGM results. Thus, we find that, even for proton projectiles, multiple ionization processes play an important role due to the availability of six relatively weakly bound electrons in the H_2O target.

Concerning the discrepancy between our results for net capture with the data of Ref. [25] in the intermediate impact-energy regime, we note that we do not expect technical difficulties in our approach at these energies. The CTMC calculations of Ref. [5] do perform a complete orientation angle average and also obtain higher results.

In Fig. 3, the charge-state correlated cross section for pure SC is compared with the experimental production of a singly ionized water molecule (H_2O^+) in coincidence with neutral hydrogen projectile formation, as measured by Gobet *et al.* [22,26] and by Luna *et al.* [27]. In contrast with the other fragments, the H_2O^+ ion is associated only with single-electron removal processes and therefore is a unique indicator for the pure SC cross section. It is not exclusive, though, since, for example, the emission of a proton together with neutral fragments also follows from single-electron removal events, and therefore the experimental data shown here represent a lower bound for pure SC.

The pure SC cross section $\tilde{\sigma}_{1,0}$ given by Eq. (31) (solid line) is consistent with the bound set by H_2O^+ measurements, whereas the direct result from the inclusive-probability analysis ($\sigma_{1,0}$, dash-dotted line) does violate the bound below 40 keV. Our result displays a somewhat different energy dependence than the CTMC prediction in Ref. [5] (blue dotted line) and the MO-based coupled-channel calculation of Ref. [7] (magenta dotted line). We find from our data between 200 and 400 keV that pure SC and transfer ionization contribute to the net capture cross section in a 2 : 1 ratio. The

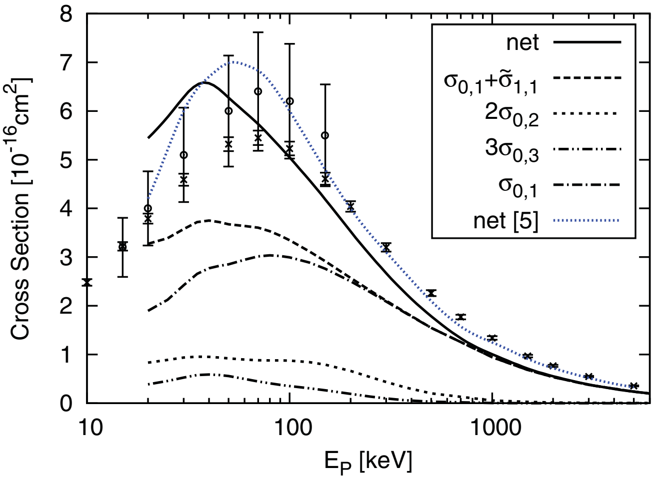

FIG. 4. (Color online) Cross sections for net ionization (net), single ionization ($\sigma_{0,1} + \tilde{\sigma}_{1,1}$), double ionization ($\sigma_{0,2}$), triple ionization ($\sigma_{0,3}$), and pure single ionization ($\sigma_{0,1}$) in proton-H_2O collisions obtained by using the inclusive-probability analysis and an average over the (0, 0, 0) and ($\pi/2$, 0, 0) molecular orientations. Experimental data are for net ionization: (×) [24], (○) [28]. The dotted (blue) line is the theoretical calculation for net ionization from Ref. [5].

cross section for transfer ionization ($\tilde{\sigma}_{1,1}$) given by Eq. (32) (dashed line) is also shown in Fig. 3. Transfer ionization is a double-electron removal process and therefore requires special attention during the fragmentation analysis (Sec. III B). It accounts for 20%–30% of the net capture cross section for all the impact energies shown in Fig. 3.

So far the emphasis has been on the projectile space. We turn to the electron continuum space in Fig. 4. The experimental net-ionization cross-section data of Rudd *et al.* [24] are shown as crosses. Their measurements were considered to be very accurate, and Gobet *et al.* [22] normalized their fragmentation data using the net ionization cross section of Ref. [24]. An independent (although less accurate) follow-up measurement by Bolorizadeh and Rudd [28] resulted in higher net cross sections (open circles). The present IPM-BGM result for the net cross section (solid line) shows 20%–30% agreement for the net ionization over much of the impact-energy range, but with a different shape. It systematically overestimates the experimental data below 60–70 keV impact energy and underestimates them at energies above 100 keV. The overestimation of net ionization at lower impact energies may be caused by the lack of dynamical response in the model. Such response effects were shown to reduce net ionization in this impact energy range in proton-Ar collisions [29].

According to the present IPM-BGM calculation, multiple-electron removal makes sizable contributions to the net cross section below 100 keV impact energy. We display in Fig. 4 cross sections for the single-, double-, and triple-ionization processes. The amount of transfer ionization is indicated by the difference between the single-ionization (SI) cross section according to Eq. (19) (i.e., $\sigma_{0,1} + \tilde{\sigma}_{1,1}$) and pure SI $\sigma_{0,1}$ in the plot. These multiple-electron removal processes have important consequences for the fragmentation cross sections, as is further discussed in Sec. III B.

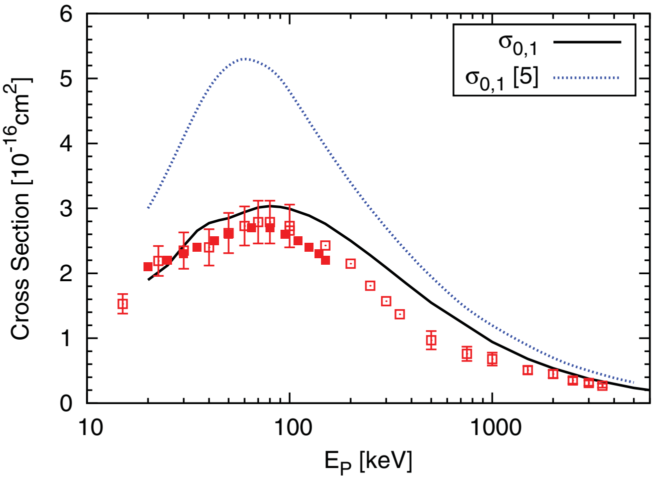

FIG. 5. (Color online) IPM-BGM cross section for pure single ionization ($\sigma_{0,1}$, solid line) compared with experimental data for H_2O^+ ion production in the ionization channel of Refs. [27] (□), [22] (■), and [30] (⊡), which set a lower bound for $\sigma_{0,1}$. The dotted (blue) line shows the theoretical result from Ref. [5].

The CTMC calculations of Ref. [5] agree well with the data of Ref. [24] at high energies and display a maximum at 60 keV. They are dominated more by SI than our results, as is shown in the next figure.

The cross section for the production of one electron in the continuum without capture ($\sigma_{0,1}$) is shown again in Fig. 5. This channel represents pure SI and can only lead to singly charged fragmentation products. Also shown in Fig. 5 are the experimental cross sections for H_2O^+ ion production in the ionization channel of Refs. [22,27,30] (squares). These data provide a lower bound for the pure SI cross section. The inclusive-probability result is seen to lie above these data for impact energies above 40 keV. The CTMC data of Ref. [5] exceed our cross section by almost a factor of two at the maximum (near 60 keV). The proximity of our result to the experimental lower bound suggests that the correct answer may lie somewhere between the two theoretical results.

In Fig. 6, we turn to the q-fold target electron loss, which in ion-atom collisions would correspond to recoil charge state production (note that the symbols used are defined in Table I). For molecular targets the situation is complicated by the fact that, for a given charge state q, different ionic species can be produced. Even the simplest channel ($q = 1$); that is, the production of H_2O^+, results not only in the emission of this molecular ion, but also in various possible fragmentation channels. As reviewed most recently by Illescas *et al.* [31], there are pathways for H_2O^+ decay, such as evaporation,

TABLE I. (Color online) Symbols for the experimental data shown in Figs. 6–8 and their references.

net : Luna [27]	⊢◇⊣	OH^+: Luna [27]	⊢○⊣	O^+: Luna [27]	⊢▽⊣
: Gobet [22]	◆	: Gobet [22]	●	: Gobet [22]	▼
: Werner [30]	◇	: Werner [30]	○	: Werner [30]	▽
H_2O^+: Luna [27]	⊢□⊣	H^+: Luna [27]	⊢△⊣	σ_+: Rudd [24]	⊢×⊣
: Gobet [22]	■	: Gobet [22]	▲		
: Werner [30]	⊡	: Werner [30]	△		

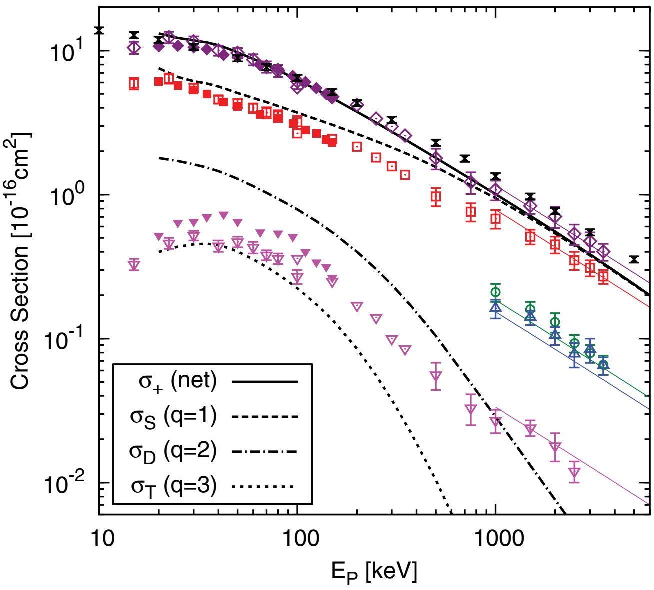

FIG. 6. (Color online) Cross sections for q-fold target electron loss in proton-H_2O collisions found by using the inclusive-probability analysis and an average over the (0, 0, 0) and ($\pi/2$, 0, 0) molecular orientations. The solid line is the net loss cross section (σ_+), which is equal to the sum of capture and ionization net cross sections (cf. Figs. 2 and 4). Below are the $q = 1$-, 2-, and 3-fold loss cross sections given by Eqs. (33)–(35). The fine solid lines for $E_P \geqslant 1$ MeV show the Bethe-Born cross sections for fragment ion production (from top to bottom: H_2O^+, OH^+, H^+, and O^+), evaluated from the net loss cross section of Ref. [8] and the population ratios of Eq. (36). Experimental data are shown for net loss [24], and for singly charged fragment ion production in the combined capture and ionization channels of Refs. [22,27,30]. The symbols for the experimental data are listed in Table I.

fission, and breakup, where the emerging singly charged fragments are OH^+, H^+, and O^+, respectively.

In the top portion of Fig. 6, the IPM-BGM cross section for net positively-charged-ion production (σ_+) obtained from adding net capture and net ionization is shown as a solid line. It is compared to the earlier data of Rudd *et al.* ([24], crosses), as well as to the more recent data for H_2O fragment production, summed over all positive ions, of Werner *et al.* [30] (center-dotted diamonds), Gobet *et al.* [22] (filled diamonds), and Luna *et al.* [27] (open diamonds). The agreement is rather good for energies up to 200 keV. For higher energies the shortfall in the prediction of net ionization in the IPM-BGM calculations becomes apparent (cf. Fig. 4). At the highest energies the theoretical cross section reaches only about 80% of the experimental values.

The IPM-BGM production cross sections for H_2O^{q+} with $q = 1, 2, 3$ are shown as dashed, dash-dotted, and dotted lines respectively in Fig. 6. They are equivalent to the net single-, double-, and triple-electron removal cross sections given by

$$\sigma_S = \tilde{\sigma}_{1,0} + \sigma_{0,1}, \tag{33}$$

$$\sigma_D = \tilde{\sigma}_{1,1} + \sigma_{0,2}, \tag{34}$$

$$\sigma_T = \sigma_{1,2} + \sigma_{0,3}. \tag{35}$$

At high projectile energies ($E_P > 1$ MeV), the net cross section is seen to be dominated by σ_S. In this energy range, it has been argued (e.g., Refs. [5,10]) that the singly charged fragment production cross sections should run in parallel scaled by the inverse of the ionization potential I_p. This behavior follows from the classical scattering limit where $\sigma_\Gamma^S \propto (E_P I_p)^{-1}$, as well as in the quantum mechanically corrected Bethe-Born approximation $\sigma_\Gamma^S \propto (E_P I_p)^{-1}(a + b \ln E_P)$ [32], or alternatively in the binary encounter Bethe model [33]. Thus, we also show the cross sections for the singly charged products according to the population ratios of

$$\sigma_{H_2O^+} : \sigma_{H^+} : \sigma_{OH^+} : \sigma_{O^+} = 68 : 16 : 13 : 3. \tag{36}$$

These population ratios are obtained in analogy to Ref. [5]; the branching ratios for fragmentation products are given according to Tan *et al.* [23] in Eqs. (27)–(30) and are combined with the MO ionization potentials I_p taken from the self-consistent field calculation for the water molecule of Ref. [19], which enter the energy representation of the BGM Hamiltonian. Our population ratios are similar to those of Refs. [5,34] but deviate from the experimental results for electron scattering at 2 keV by Schutten *et al.* [35] which favor the production of H^+ over OH^+. The Born limit for the net cross section is taken from Ref. [8]. It lies above the IPM-BGM result but below the experimental data of Rudd *et al.* [24].

We find at intermediate and lower energies that the situation is less clear (i.e., more interesting). From the theoretical prediction of nontrivial multiple (q-fold) target ionization it is evident that a simple analysis based on the fixed population ratios is not sufficient to explain the experimental data for fragmentation products. Thus, we show only two channels in Fig. 6; the H_2O^+ production cross section serves as an experimental lower bound for σ_S. At the lowest impact energies where capture dominates, our calculations do touch the bound, which indicates that they overestimate multiple-electron ionization. We also display the experimental data for positive-oxygen-ion (O^+) production in this graph, which should serve as an upper bound for σ_T because H_2O^{3+} decays into two protons and one O^+ (assuming that the formation of O^{2+} is very unlikely), while a part of σ_S also contributes to the O^+ production. At the lower energies, σ_T reaches the level of the observed O^+ production. The compression of the range of fragmentation cross sections when one goes from higher to lower impact energies is evidence of the fact that some of the enhancement in the O^+ production must come from fragmentation following H_2O^{q+} production with $q > 1$. A more detailed look at the fragmentation cross sections follows in the next section.

B. Fragmentation cross sections

In Fig. 7, we compare the cross sections for the production of singly charged fragments with experimental results. The calculations are based on the exclusive single-vacancy production cross section for each MO (Sec. II B1) and the branching ratios as given by Tan *et al.* [23] (Sec. II B3). The purpose of this comparison is to highlight the breakdown of the perturbative single-vacancy production model at low energies where multiple processes play an important role. For example, vacancy production in the outermost orbitals

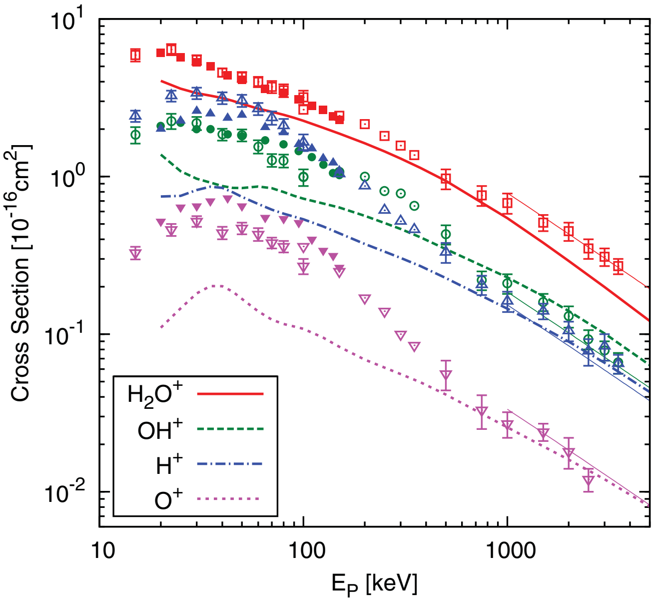

FIG. 7. (Color online) Fragmentation cross sections for proton-H_2O collisions given by Eqs. (27)–(30), based on the inclusive-probability analysis and an average over the (0, 0, 0) and ($\pi/2$, 0, 0) molecular orientations. Experimental data are shown for singly charged fragment ion production in the combined capture and ionization channels of Refs. [22,27,30]. The fine solid lines for $E_P \geqslant 1$ MeV show the Bethe-Born cross sections for fragment ion production (cf. Fig. 6). The symbols for the experimental data are listed in Table I.

$(1b_1$ and $3a_1)$ is associated completely with H_2O^+ production according to Eqs. (27)–(30). Obviously, this channel can only be reached if the vacancy is produced exclusively in one or the other orbital. The other singly charged ions are produced by single-vacancy production but can also be produced by multiple-electron removal processes. It is clear (particularly from the O^+-channel data) that multiple-electron removal events play a substantial role when impact energies are below 500 keV (cf. Fig. 6).

At high energies, the theoretical fragmentation data in Fig. 7 deviate significantly from the Bethe-Born limit (shown with fine solid lines above 1 MeV as in Fig. 6). This is caused most likely by the limited orientation average. The exclusive single-vacancy production analysis, which is the correct basis for applying the branching ratios of Tan *et al.* [23], is based on MO-specific probabilities which are not averaged properly over all orientations as we use the two orientations (0,0,0) and ($\pi/2$,0,0) only. Figure 7 shows that averaging just two orientations is not sufficient for extracting information about exclusive single-vacancy probabilities, even though it results in reasonable cross sections for those cases, in which all the different MO contributions are added.

At lower impact energies, the exclusive single-vacancy analysis falls short in all channels. Only at intermediate energies is the production of H_2O^+ predicted reasonably well, the other three channels do not show the steep rise toward lower energies observed in the experimental data. On the one hand, one can question to what extent the branching ratios of Tan *et al.* [23] are applicable outside the perturbative regime. At energies below 100 keV the exclusive single-vacancy analysis even fails to predict the H_2O^+ production cross section; this points to yet another problem (i.e., misidentification of unphysical double-electron capture in the inclusive-probability analysis). It is not straightforward to apply the pragmatic corrections analogous to Eqs. (31) and (32) in the exclusive single-vacancy production calculation.

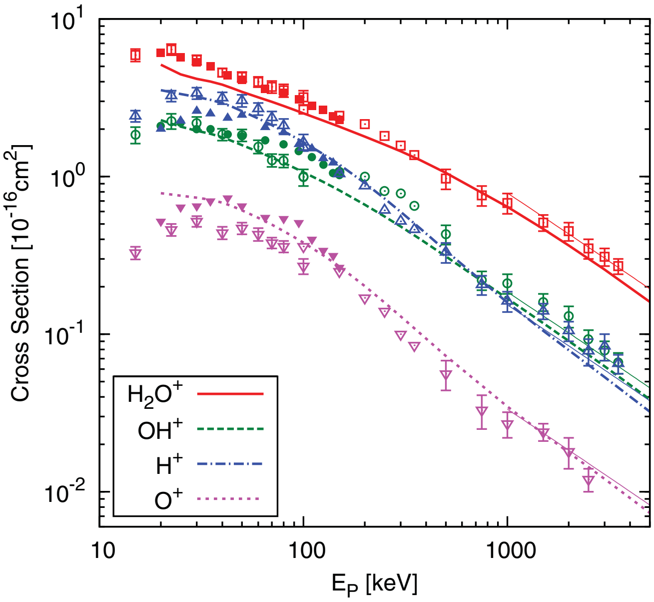

FIG. 8. (Color online) Same as Fig. 7, but theoretical calculations are based on the fragmentation model given by Eqs. (37)–(40).

Therefore, we conclude that the fragmentation cross sections based on Eqs. (27)–(30) are not very useful below 500 keV. In the following we carry out an alternative calculation of fragmentation based upon q-fold target electron removal and by the use of Eqs. (31) and (32) to remove the unphysical double-electron capture.

Figure 8 shows the cross section including the effects of multiple-electron removal processes without differentiating between capture and transfer to the continuum. We retain the H_2O^+ fragmentation model from Eq. (36) for single-electron removal and assume for simplicity that only the following fragmentation reactions are important for double- and triple-electron removal:

$$\begin{aligned}
H_2O^{2+} &\xrightarrow{60\%} H^+ + OH^+,\\
H_2O^{2+} &\xrightarrow{20\%} H^+ + H^+ + O^0,\\
H_2O^{2+} &\xrightarrow{20\%} H^+ + H^0 + O^+,\\
H_2O^{3+} &\xrightarrow{100\%} H^+ + H^+ + O^+.
\end{aligned}$$

Then, we have

$$\sigma_{H_2O^+} = 0.68\sigma_S, \tag{37}$$

$$\sigma_{OH^+} = 0.16\sigma_S + 0.6\sigma_D, \tag{38}$$

$$\sigma_{H^+} = 0.13\sigma_S + 1.2\sigma_D + 1.0\sigma_T, \tag{39}$$

$$\sigma_{O^+} = 0.03\sigma_S + 0.2\sigma_D + 0.5\sigma_T, \tag{40}$$

where σ_S, σ_D, and σ_T are given by Eqs. (33)–(35), respectively, and the σ_T contributions have been multiplied by a factor of 0.5 to account for the fact that the IPM overestimates triple processes [36], as seen by comparing our data with the coincidence measurements of Werner *et al.* [30].

The fragmentation model of Eqs. (37)–(40) is based upon the following assumptions: the distribution of singly charged ($q = 1$) target production over the singly ionized fragments is taken from the high-energy limit (as shown in Fig. 6) and assumed to be applicable at all projectile energies. Double-electron removal ($q = 2$) is modelled to reflect the coincidence measurements of Werner *et al.* [30] and to produce a balance between the amounts of H^+ and OH^+ ions in accord with observations [36]. Triple-electron removal ($q = 3$) is assumed to be predominantly associated with the production of two protons and a singly charged oxygen atom.

The fragmentation cross sections in Fig. 8 show much better agreement with the Bethe-Born limit (shown with fine solid lines above 1 MeV) than those given in Fig. 7, since the limited orientation average affects the individual-MO cross sections but not the charge-state correlated cross sections, on which Eqs. (37)–(40) are built. When moving toward intermediate energies we notice very good agreement with the experimental data: the O^+ channel is reproduced rather well, and the crossing of the H^+ and OH^+ cross sections is predicted with some accuracy. At the lower energies we find a small shortfall in the H_2O^+ fragment production, while the other channels are described reasonably well. The shortfall of the H_2O^+ channel could mean that the assumption of projectile-energy-independent population ratios for the single-electron removal is showing its limitations. It could also mean that the present calculation over-predicts double-electron removal; transfer ionization in particular may be overestimated in our IPM. A physical reason for a change in the population ratios when going from higher to lower impact energies is that slow collisions will provide time for electronic relaxation, possibly resulting in less fragmentation (i.e., more H_2O^+ production).

IV. CONCLUSION

In this work we have presented results and laid out more details from the IPM-BGM calculation for collisions of protons with a molecule that has a simple but nontrivial geometry. First results for net capture and ionization cross sections were shown previously in Ref. [11] to agree with experimental data at proton energies between 20 and 5000 keV. The approach avoids the explicit use of multicenter potential energy matrix elements in the time-dependent calculation by going into an energy representation of the target Hamiltonian. The propagation of single-particle MOs is performed within the previously developed BGM, and carried out in a representation in terms of atomic oxygen eigenstates derived from DFT at the level of the optimized potential method, which includes exact exchange but no correlation.

The present paper extends the results to compare with experimental data for charge-state correlated cross sections, as well as fragmentation data following q-fold electron removal from the target. The work shows that multiple-ionization processes should not be ignored, even though they may be over-predicted within an IPM framework.

We show how a quantum many-electron analysis of the evolved Slater determinant of single-electron MOs allows us to use the high-energy-limit branching ratios of Tan *et al.* [23] to calculate cross sections for H_2O fragmentation products at intermediate and high energies, where multiple-electron processes can be neglected. This analysis fails at lower impact energies due to the importance of multiple-electron removal processes, particularly transfer ionization. Unfortunately, our own calculation based on this analysis does not reproduce the high-energy Bethe-Born limit for technical reasons, since we do not perform a complete average over molecular orientations. This causes errors in the calculation of individual MO-vacancy production, but not in cross sections for which all the MO contributions are added. A model based on such cross sections that complements the disintegration model of H_2O^+ with populations of OH^+, H^+, and O^+ following two- and three-electron removal is shown to roughly agree with experimental fragmentation yields of Refs. [22,27,30], except for the H_2O^+ channel at low impact energies where the model calculation falls short.

Overall one can argue that the calculations are good to make fragment yield predictions at the 20%–30% level or better. The prediction of fragmentation following q-fold electron removal at low to intermediate energies represents a first theoretical analysis of proton-H_2O collisions, but we note that the modeling of fragmentation events following multiple-electron removal is not new [1,10].

We also compared our results to another nonperturbative method, namely the three-center CTMC calculations of Illescas *et al.* [5]. We find some overall agreement, but also important discrepancies. In particular, we find that our single-ionization cross section is below their model prediction, but note that their net ionization yield is rather high; that is, that they also predict strong multiple ionization at moderate energies.

We limited the present study of fragmentation due to q-fold electron removal without differentiating with respect to capture and pure ionization, since the normalization of experimental data at lower energies (10–150 keV) in Refs. [22,27] is somewhat ambiguous in how transfer ionization is included, resulting in discrepancies between the experimental data from the two groups. We have presented a detailed comparison together with the justification of our fragmentation model in Ref. [36].

ACKNOWLEDGMENTS

This work was supported by NSERC Canada and by SHARCNET.

APPENDIX

A two-center basis is most conveniently discussed in an inertial reference frame whose origin coincides with the c.m. of both centers (i.e., of the projectile and the oxygen nucleus in the present case). If we denote the number of (atomic) target and projectile states by N_T and N_P, respectively, a Galilean-invariant two-center AO basis can be written as

$$\phi_j^0(\vec{r}) = \begin{cases} \phi_j(\vec{r}_T)\exp(i\vec{v}_T\cdot\vec{r}) & \text{if } j \leqslant N_T \\ \phi_j(\vec{r}_P)\exp(i\vec{v}_P\cdot\vec{r}) & \text{if } N_T < j \leqslant N_T + N_P, \end{cases} \tag{A1}$$

with $\vec{r}_T$, $\vec{r}_P$, and $\vec{r}$ denoting the position vectors of the electron with respect to the target, the projectile, and the c.m., respectively, and $\vec{v}_T$ and $\vec{v}_P$ being the constant velocities of the atomic target and projectile centers with respect to the c.m. If the AOs fulfill stationary eigenvalue equations for the (atomic) target and projectile Hamiltonians

$$\hat{H}^{T,P} = -\tfrac{1}{2}\nabla^2 + V^{T,P} \tag{A2}$$

in the (moving) target and projectile reference frames, respectively, the states defined by Eq. (A1) satisfy

$$(\hat{H}^{T,P} - i\partial_t)\,|\phi_j^0\rangle = g_j\,|\phi_j^0\rangle, \tag{A3}$$

with

$$g_j = \varepsilon_j + \frac{v_{T,P}^2}{2} \tag{A4}$$

and the atomic energy eigenvalues ε_j. Similarly, the MOs $|\Gamma_{\alpha\beta\gamma}\rangle$ which move with the target system satisfy

$$\left(\hat{H}^T_{\alpha\beta\gamma} - i\partial_t\right)|\Gamma_{\alpha\beta\gamma}\rangle = f_\Gamma|\Gamma_{\alpha\beta\gamma}\rangle, \quad f_\Gamma = \epsilon_\Gamma + \tfrac{1}{2}v_T^2, \tag{A5}$$

with the molecular energy eigenvalues ϵ_Γ [cf. Eqs. (3) and (7)].

In the following, we use the short-hand notation $|j0\rangle$ for the jth state of Eq. (A1) and

$$|jJ\rangle = W_P^J|j0\rangle \tag{A6}$$

for the BGM pseudostates, which are constructed by operating with the regularized projectile potential

$$W_P = \frac{1}{r_P}(1 - e^{-r_P}), \tag{A7}$$

on the set of target AOs [12,15]. The solution of the single-particle equations (1) involves the calculation of the interaction matrix elements [cf. Eq. (6)]

$$M_{kj}^{KJ}(\alpha,\beta,\gamma) = \langle kK|\hat{H}^T_{\alpha\beta\gamma} + V^P(t) - i\partial_t|jJ\rangle \tag{A8}$$

for all TC-BGM basis states. We rewrite M_{kj}^{KJ} by using similar arguments as in Appendix D of Ref. [37]:

$$\begin{aligned} M_{kj}^{KJ}(\alpha,\beta,\gamma) = {}& \langle kK|\frac{1}{2}KJ\left(\frac{\nabla W_P}{W_P}\right)^2 + \frac{K}{K+J}V_{\bar{j}} \\ & + \frac{J}{K+J}V_{\bar{k}}|jJ\rangle - \frac{J}{K+J}i\partial_t\langle kK|jJ\rangle \\ & + m_{kj}^{KJ}(\alpha,\beta,\gamma), \end{aligned} \tag{A9}$$

$$m_{kj}^{KJ}(\alpha,\beta,\gamma) = \frac{K}{K+J}\langle k0|W_P^{K+J}\left(\hat{H}^T_{\alpha\beta\gamma} + V^P - V_{\bar{j}} - i\partial_t\right)|j0\rangle + \frac{J}{K+J}\langle j0|W_P^{K+J}\left(\hat{H}^T_{\alpha\beta\gamma} + V^P - V_{\bar{k}} - i\partial_t\right)|k0\rangle^*, \tag{A10}$$

where for $j \leqslant N_T$ we set $V_{\bar{j}} = V^P$ and $V_j = V^T$, while for $j > N_T$ we set $V_{\bar{j}} = V^T$ and $V_j = V^P$. Inserting $\sum_\Lambda |\Lambda_{\alpha\beta\gamma}\rangle\langle\Lambda_{\alpha\beta\gamma}| = \hat{1}$ and using Eq. (A5), which is equivalent to introducing the spectral representation (7), turns Eq. (A10) into

$$\begin{aligned} m_{kj}^{KJ}(\alpha,\beta,\gamma) = {}& \sum_\Lambda \left[\frac{K}{K+J}\langle k0|W_P^{K+J}\left(\hat{H}^T_{\alpha\beta\gamma} + V^P - V_{\bar{j}} - i\partial_t\right)|\Lambda_{\alpha\beta\gamma}\rangle\langle\Lambda_{\alpha\beta\gamma}|j0\rangle \right. \\ & \left. + \frac{J}{K+J}\langle j0|W_P^{K+J}\left(\hat{H}^T_{\alpha\beta\gamma} + V^P - V_{\bar{k}} - i\partial_t\right)|\Lambda_{\alpha\beta\gamma}\rangle^*\langle\Lambda_{\alpha\beta\gamma}|k0\rangle^*\right] \\ = {}& \sum_\Lambda \left\{\frac{K}{K+J}\left[\langle k0|W_P^{K+J}(V^P - V_{\bar{j}} + f_\Lambda)|\Lambda_{\alpha\beta\gamma}\rangle\langle\Lambda_{\alpha\beta\gamma}|j0\rangle - \langle k0|W_P^{K+J}|\Lambda_{\alpha\beta\gamma}\rangle i\partial_t\langle\Lambda_{\alpha\beta\gamma}|j0\rangle\right] \right. \\ & \left. + \frac{J}{K+J}\left[\langle k0|\Lambda_{\alpha\beta\gamma}\rangle\langle\Lambda_{\alpha\beta\gamma}|W_P^{K+J}(V^P - V_{\bar{k}} + f_\Lambda)|j0\rangle + (i\partial_t\langle k0|\Lambda_{\alpha\beta\gamma}\rangle)\langle\Lambda_{\alpha\beta\gamma}|W_P^{K+J}|j0\rangle\right]\right\}. \end{aligned} \tag{A11}$$

In the next step we rewrite the time derivatives of the overlap matrix elements that occur in the second and fourth terms of Eq. (A11) by using the single-center expansion (8) of the MOs:

$$i\partial_t\langle\Lambda_{\alpha\beta\gamma}|j0\rangle = \sum_s d^\Lambda_{s,\alpha\beta\gamma}i\partial_t\langle s|j0\rangle = \sum_s d^\Lambda_{s,\alpha\beta\gamma}\langle s|(V_j - V^T + g_s - g_j)|j0\rangle = \sum_s\langle\Lambda_{\alpha\beta\gamma}|s\rangle\langle s|(V_j - V^T + g_s - g_j)|j0\rangle, \tag{A12}$$

and similarly

$$i\partial_t\langle k0|\Lambda_{\alpha\beta\gamma}\rangle = \sum_s d^\Lambda_{s,\alpha\beta\gamma}i\partial_t\langle k0|s\rangle = \sum_s\langle\Lambda_{\alpha\beta\gamma}|k0\rangle\langle k0|(V^T - V_k + g_k - g_s)|s\rangle. \tag{A13}$$

This yields

$$\begin{aligned} m_{kj}^{KJ}(\alpha,\beta,\gamma) = \sum_\Lambda \left\{\frac{K}{K+J}\left[\langle k0|W_P^{K+J}(V^P - V_{\bar{j}} + f_\Lambda)|\Lambda_{\alpha\beta\gamma}\rangle\langle\Lambda_{\alpha\beta\gamma}|j0\rangle \right.\right. \\ \left. - \sum_s\langle k0|W_P^{K+J}|\Lambda_{\alpha\beta\gamma}\rangle\langle\Lambda_{\alpha\beta\gamma}|s\rangle\langle s|(V_j - V^T + g_s - g_j)|j0\rangle\right] \end{aligned}$$

$$+\frac{J}{K+J}\bigg[\langle k0|\Lambda_{\alpha\beta\gamma}\rangle\langle\Lambda_{\alpha\beta\gamma}|W_P^{K+J}(V^P - V_{\bar{k}} + f_\Lambda)|j0\rangle + \sum_s \langle k0|(V^T - V_k + g_k - g_s)|s\rangle\langle s|\Lambda_{\alpha\beta\gamma}\rangle\langle\Lambda_{\alpha\beta\gamma}|W_P^{K+J}|j0\rangle\bigg]\bigg\}. \tag{A14}$$

Using completeness relations for both the single-center basis $\{|s\rangle\}$ and the MOs $\{|\Lambda_{\alpha\beta\gamma}\rangle\}$ allows us to cast Eq. (A14) into the form

$$m_{kj}^{KJ}(\alpha,\beta,\gamma) = \frac{K}{K+J}\left(\sum_\Lambda f_\Lambda \langle k0|W_P^{K+J}|\Lambda_{\alpha\beta\gamma}\rangle\langle\Lambda_{\alpha\beta\gamma}|j0\rangle + g_j\langle k0|W_P^{K+J}|j0\rangle - \sum_s g_s\langle k0|W_P^{K+J}|s\rangle\langle s|j0\rangle\right) + \frac{J}{K+J}\left(\sum_\Lambda f_\Lambda\langle k0|\Lambda_{\alpha\beta\gamma}\rangle\langle\Lambda_{\alpha\beta\gamma}|W_P^{K+J}|j0\rangle + g_k\langle k0|W_P^{K+J}|j0\rangle - \sum_s g_s\langle k0|s\rangle\langle s|W_P^{K+J}|j0\rangle\right). \tag{A15}$$

In the last step we use again the single-center expansion (8) of the MOs and obtain

$$m_{kj}^{KJ}(\alpha,\beta,\gamma) = \frac{K}{K+J}\left(\sum_\Lambda f_\Lambda \sum_{s,t} d^\Lambda_{s,\alpha\beta\gamma} d^\Lambda_{t,\alpha\beta\gamma}\langle k0|W_P^{K+J}|s\rangle\langle t|j0\rangle + g_j\langle k0|W_P^{K+J}|j0\rangle - \sum_s g_s\langle k0|W_P^{K+J}|s\rangle\langle s|j0\rangle\right) + \frac{J}{K+J}\left(\sum_\Lambda f_\Lambda\sum_{s,t} d^\Lambda_{s,\alpha\beta\gamma} d^\Lambda_{t,\alpha\beta\gamma}\langle k0|s\rangle\langle t|W_P^{K+J}|j0\rangle + g_k\langle k0|W_P^{K+J}|j0\rangle - \sum_s g_s\langle k0|s\rangle\langle s|W_P^{K+J}|j0\rangle\right), \tag{A16}$$

which involves only energy values, expansion coefficients, and two-center overlap and potential matrix elements. Note that Eqs. (A9) and (A16) would be equivalent to using the spectral representation of the molecular Hamiltonian directly in Eq. (A8) as indicated in Eq. (9) if the set of MOs $\{|\Lambda_{\alpha\beta\gamma}\rangle\}$ and the single-center basis $\{|s\rangle\}$ were complete. However, in practice they are not, and one cannot expect to obtain identical results from both procedures. The main reason why we implemented the seemingly more cumbersome approach described in this appendix is that Eqs. (A9) and (A16) are completely symmetric with respect to the projectile and target potentials which define the two-center basis $\{|j0\rangle\}$. This is crucial to ensure that the interaction matrix elements vanish at large separations between projectile and target and the asymptotic transition probabilities become stable.

[1] H. Luna and E. C. Montenegro, Phys. Rev. Lett. **94**, 043201 (2005).

[2] P. M. Y. Garcia, G. M. Sigaud, H. Luna, A. C. F. Santos, E. C. Montenegro, and M. B. Shah, Phys. Rev. A **77**, 052708 (2008).

[3] R. Cabrera-Trujillo, E. Deumens, Y. Öhrn, O. Quinet, J. R. Sabin, and N. Stolterfoht, Phys. Rev. A **75**, 052702 (2007).

[4] C. Champion, D. Oubaziz, H. Aouchiche, Y. V. Popov, and C. Dal Cappello, Phys. Rev. A **81**, 032704 (2010).

[5] C. Illescas, L. F. Errea, L. Méndez, B. Pons, I. Rabadán, and A. Riera, Phys. Rev. A **83**, 052704 (2011).

[6] A. Dubois, S. Carniato, P. D. Fainstein, and J. P. Hansen, Phys. Rev. A **84**, 012708 (2011).

[7] P. M. M. Gabás, L. F. Errea, L. Méndez, and I. Rabadán, Phys. Rev. A **85**, 012702 (2012).

[8] O. Boudrioua, C. Champion, C. Dal Cappello, and Y. V. Popov, Phys. Rev. A **75**, 022720 (2007).

[9] B. Gervais, M. Beuve, G. H. Olivera, and M. E. Galassi, Radiat. Phys. Chem. **75**, 493 (2007).

[10] E. C. Montenegro, J. Phys.: Conf. Ser. **194**, 012049 (2009).

[11] H. J. Lüdde, T. Spranger, M. Horbatsch, and T. Kirchner, Phys. Rev. A **80**, 060702(R) (2009).

[12] O. J. Kroneisen, H. J. Lüdde, T. Kirchner, and R. M. Dreizler, J. Phys. A **32**, 2141 (1999).

[13] T. Kirchner, H. J. Lüdde, M. Horbatsch, and R. M. Dreizler, Phys. Rev. A **61**, 052710 (2000).

[14] T. Kirchner, A. C. F. Santos, H. Luna, M. M. Sant'Anna, W. S. Melo, G. M. Sigaud, and E. C. Montenegro, Phys. Rev. A **72**, 012707 (2005).

[15] M. Zapukhlyak, T. Kirchner, H. J. Lüdde, S. Knoop, R. Morgenstern, and R. Hoekstra, J. Phys. B **38**, 2353 (2005).

[16] T. Kirchner, H. J. Lüdde, and M. Horbatsch, Recent Res. Dev. Phys. **5**, 433 (2004).

[17] T. Kirchner, M. Murakami, M. Horbatsch, and H. J. Lüdde, J. Phys.: Conf. Ser. (2012) (to be published).

[18] E. Engel and S. H. Vosko, Phys. Rev. A **47**, 2800 (1993).

[19] S. Aung, R. M. Pitzer, and S. I. Chan, J. Chem. Phys. **49**, 2071 (1968).

[20] H. J. Lüdde and R. M. Dreizler, J. Phys. B **18**, 107 (1985).

[21] T. Kirchner, L. Gulyás, H. J. Lüdde, E. Engel, and R. M. Dreizler, Phys. Rev. A **58**, 2063 (1998).

[22] F. Gobet, S. Eden, B. Coupier, J. Tabet, B. Farizon, M. Farizon, M. J. Gaillard, M. Carré, S. Ouaskit, T. D. Märk, and P. Scheier, Phys. Rev. A **70**, 062716 (2004).

[23] K. H. Tan, C. E. Brion, P. E. van der Leeuw, and M. J. van der Wiel, Chem. Phys. **29**, 299 (1978).

[24] M. E. Rudd, T. V. Goffe, R. D. DuBois, and L. H. Toburen, Phys. Rev. A **31**, 492 (1985).

[25] L. H. Toburen, M. Y. Nakai, and R. A. Langley, Phys. Rev. **171**, 171 (1968).

[26] F. Gobet, B. Farizon, M. Farizon, M. J. Gaillard, M. Carré, M. Lezius, P. Scheier, and T. D. Märk, Phys. Rev. Lett. **86**, 3751 (2001).

[27] H. Luna, A. L. F. de Barros, J. A. Wyer, S. W. J. Scully, J. Lecointre, P. M. Y. Garcia, G. M. Sigaud, A. C. F. Santos, V. Senthil, M. B. Shah, C. J. Latimer, and E. C. Montenegro, Phys. Rev. A **75**, 042711 (2007).

[28] M. A. Bolorizadeh and M. E. Rudd, Phys. Rev. A **33**, 888 (1986).

[29] T. Kirchner, M. Horbatsch, and H. J. Lüdde, Phys. Rev. A **66**, 052719 (2002).

[30] U. Werner, K. Beckord, J. Becker, and H. O. Lutz, Phys. Rev. Lett. **74**, 1962 (1995).

[31] E. C. Montenegro, S. W. J. Scully, J. A. Wyer, V. Senthil, and M. B. Shah, J. Electron Spectrosc. Relat. Phenom. **155**, 81 (2007).

[32] I. D. Kaganovich, E. A. Startsev, and R. C. Davidson, Phys. Rev. A **68**, 022707 (2003).

[33] W. Hwang, Y. K. Kim, and M. E. Rudd, J. Chem. Phys. **104**, 2956 (1996).

[34] J. H. Miller, W. E. Wilson, S. T. Manson, and M. E. Rudd, J. Chem. Phys. **86**, 157 (1987).

[35] J. Schutten, F. J. de Heer, H. R. Moustafa, A. J. H. Boerboom, and J. Kistemaker, J. Chem. Phys. **44**, 3924 (1966).

[36] M. Murakami, T. Kirchner, M. Horbatsch, and H. J. Lüdde, Phys. Rev. A (accepted).

[37] H. J. Lüdde, A. Henne, T. Kirchner, and R. M. Dreizler, J. Phys. B **29**, 4423 (1996).